Interaction of ultrashort-laser pulses with induced undercritical plasmas in fused silica

Jeremy R. Gulley[*]

Department of Biology and Physics, Kennesaw State University, Kennesaw, Georgia 30144, USA

Sebastian W. Winkler and William M. Dennis[†]

Department of Physics and Astronomy, The University of Georgia, Athens, Georgia 30602, USA

Carl M. Liebig[‡] and Razvan Stoian

Laboratoire Hubert Curien, UMR 5516 CNRS, Université de Lyon, Université Jean Monnet, F-42000 Saint Etienne, France

Ultrafast light-material interactions near the damage threshold are often studied using postmortem analysis of damaged dielectric materials. Corresponding simulations of ultrashort pulse propagation through the material are frequently used to gain additional insight into the processes leading to such damage. However, comparison between such experimental and numerical results is often qualitative, and pulses near to but not exceeding the damage threshold leave no permanent changes in the material for postmortem analysis. In this article, a series of experiments is presented that measures the near- and far-field properties of a 140-fs laser pulse after propagation through a fused silica sample in which a noncritical electron plasma was generated. Concurrently, results from simulations in which the laser pulse was numerically constructed according to the nearfield beam profile and frequency resolved optical gating (FROG) trace are presented. It is found that to extract a quantitative comparison of such data, cylindrical symmetry of the laser pulse in simulations should be abandoned in favor of a fully 3 + 1D Cartesian representation. Further comparison of experimental and calculated damage thresholds shows that time-corrective effects predicted by the Drude model play a critical role in the physics of both pulse evolution and plasma formation. The influence of resulting spatiotemporal dependences of the pulse in far-field measurements leads to unretrievable FROG traces. However, it is shown through both simulation and experiment that the use of an appropriate beam aperture will eliminate this effect when measuring the temporal pulse amplitude.

PACS number(s): 42.65.Re, 52.38.Hb, 52.38.Dx

I. INTRODUCTION

With the industrial need for precise modification of optical materials growing rapidly, the ultrashort laser pulse interaction with these materials is gaining increased attention [1–12]. It has been shown that the use of ultrashort laser pulses allows for a variety of modifications to highly localized regions both on the surface and in the bulk of transparent materials [13–19]. An understanding of the field-matter interactions leading to such modifications is essential for the development of new applications.

The initial process in ultrafast material modification of transparent dielectrics is the generation of a free-electron gas [20]. When the electron gas is sufficiently dense it becomes highly absorbent, leading to a significant transfer of energy from the laser pulse into the material. Depending on the amount of energy transferred, this can lead to a change in lattice structure, melting, or ablation, any of which can result in the destruction of the material [2,7,21]. While damage is a visible record of the pulse-plasma interaction, it is the initial interaction itself and resulting ultrafast free-electron generation that must be understood and controlled when using femtosecond pulses.

Numerous studies have included a postmortem analysis of the optical damage on the surface and in the bulk and used a wide variety of computer simulations to interpret the results [8,19,22–27]. While those studies have greatly advanced the understanding of the induced-plasma processes and the nonlinear effects inside the material above the damage threshold, physical processes leading up to the damage regime are not accessible with many of these experimental techniques. For pulses below the damage threshold the material typically shows very little plasma emission and no optical modification that can be investigated. Using double- or multipulse trains, it has been shown that a noncritical electron plasma can be produced well below the permanent damage threshold [18,19,28]. Results from simulations that access those regimes are very important to the study of this interaction and should be confirmed by experiment.

This work has two primary goals: first, to examine the effects of spatiotemporal field asymmetries in laser pulse-plasma evolution and to quantify the effects of these asymmetries on measurements of the far field and, second, to merge experimental data directly with simulation to test the physical significance of recently derived corrective terms to the standard Drude model description of ultrashort-pulse interactions with noncritical electron plasmas [30]. In the progress of this work, the first goal is used as an integral part of validating the results of the second goal. To better understand the interaction of the generated-noncritical electron gas with the laser pulse, we present a series of experiments and numerical simulations that investigate the change in the ultrashort pulse as a result of

[*]jgulley@kennesaw.edu

[†]bill@physast.uga.edu

[‡]Present address: Azimuth Corporation, 3005 Hobson Way, Building 651, WPAFB, OH 45433, USA

its interaction with the electron plasma. In the experiments presented, the propagation effects of a 140-fs full width at half-maximum (FWHM) laser pulse with a central wavelength of 800 nm through a 200-μm fused silica sample under loose focusing conditions were investigated. To ensure the accuracy of computational models, the simulations presented in this article were constructed using experimentally measured beam profiles and pulse shapes to create a fully three-dimensional (3D) digital representation of the laser pulse.

The results are presented as follows: First, the multishot damage threshold of the experiment is compared with the single-shot damage threshold prediction of the simulation. Time-corrective effects predicted by the Drude model that are often improperly included in ultrashort pulse simulations are shown to play a critical role in the physics of both pulse evolution and plasma generation. Second, to validate the computer simulation results, the beam profiles recorded in the experiment and from the computer simulation are compared. Finally, simulated and experimental frequency resolved optical gating (FROG) measurements of the far field are analyzed. It is shown that the effects from spatiotemporal dependences in the field (predicted by the simulations) can be seen in the experimental FROG traces of the field. Those dependences are reduced when using an aperture, which allows the retrieval of the field amplitude as a function of time.

II. EXPERIMENTAL SETUP

Two different laser systems were used, both cw-pumped Ti:sapphire oscillators (Spectra-Physics Tsunami, Coherent Inc.; Vitesse) with a regenerative multipass Ti-sapphire amplifier (Clark MXR CPU; Thales Laser; Concerto), producing pulses of 120–150 fs at a central wavelength of 800 nm with a repetition rate of 1 kHz. The laser beam was apertured in both cases and passed through an attenuator to regulate the input pulse power. After the attenuator the input beam profile was measured and the beam was focused onto the front surface of the sample with a 25-cm-focal-length lens (Fig. 1). Between the lens and the sample the input power was measured. The sample was made of 200-μm-thick fused silica that was polished on both sides. These experiments were performed at atmospheric pressure in air. After the sample, the beam was recollimated using a second 25-cm-focal-length lens. Following the second lens, the final beam profiles were measured and the beam was apertured again. To measure the pulse shape after transmission through the sample, a second-harmonic-generation (SHG) FROG experiment was used [29].
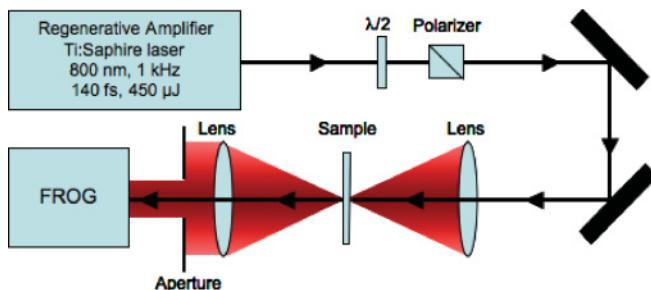

FIG. 1. (Color online) Experimental setup.

III. SIMULATION

To simulate the propagation of a linearly polarized laser pulse, a modified nonlinear Schrödinger equation (NLSE) is solved for the complex field envelope $A(x,y,z,\tau)$ [30]:

$$
\begin{aligned}
\frac{\partial A}{\partial z} = {} & \frac{i}{2k_0}\hat{T}^{-1}\nabla_\perp^2 A + i\hat{D}_b A + i\frac{k_0 n_2}{n_0}(1-f_r)\hat{T} I A \\
& + i\frac{k_0 n_2}{n_0}f_r \hat{T}\left[\int_{-\infty}^{\tau} d\tau' R(\tau-\tau')I(\tau')\right]A \\
& - \frac{W_{\mathrm{PI}}U}{2I}A - \frac{\sigma}{2}(1+i\omega_0\tau_c)\hat{G}^{-1}[\rho A].
\end{aligned} \tag{1}
$$

This modified NLSE is solved simultaneously with the multirate equation describing the evolution of the free-carrier plasma ρ as proposed by Rethfeld [31]. In both equations the photoionization rate W_{PI} is calculated using the Keldysh model [32] with a reduced electron-hole mass of half the electron rest mass and the one-photon absorption cross section σ as derived from the Drude model [30,33]. In solving the multirate equation we also assume an exponential loss of free carriers from the conduction band with a recombination time of 150 fs [19,34].

The variables and parameters in Eq. (1) are summarized in Table I. The first two terms in Eq. (1) describe the diffraction and dispersion of the field due to the bound charges, respectively. In this article, only group velocity dispersion was included in the second term due to the fact that the propagation distance was many orders of magnitude less than the dispersion distance of any higher order. Linear absorption was neglected. The third term in Eq. (1) accounts for the instantaneous Kerr effect and self-steepening, while the fourth term is the contribution of stimulated Raman scattering to the nonlinear polarization. The fifth term accounts for photoionization and the last term describes the free-carrier effects as calculated by the Drude model [30]. Note that the field envelope is related to the real electric field as a function of space and time by $E(\vec{x},t) = (1/2)A(\vec{x},t)\exp[i(k_0 z - \omega_0 t)] + \mathrm{c.c.}$

Computer simulation results presented here were obtained using a 256×256 spatial grid with 512 time points. The spatial resolution was chosen to be $\delta x = 10w_{xy}/256$ and the temporal resolution was chosen to be $\delta t = 10\tau_0/512$, where w_{xy} and τ_0 are the approximate $1/e^2$ widths of the beam and pulse, respectively. Pulse parameters were chosen to be as representative of the experimental data as possible. The pulse shape and the temporal phase for the simulations were obtained from a measured laser pulse, corresponding to the initial experimental conditions, using SHG-FROG [29]. The initial beam profile was measured in the experiment before the first lens. This beam profile had sharp edges (due to the clipping by the detector), which were extrapolated and smoothed out at the edges using a super-Gaussian windowing function. The smoothed beam profile was interpolated to the 256×256 grid size and then Fourier transformed to simulate the focusing of the beam onto the sample surface, at which point the 3D input field envelope $A(x,y,\tau,z=0)$ was numerically constructed from the Fourier transformed beam profile and the field retrieved from the measured SHG-FROG trace. Pulse energies chosen for the computer simulations span the same energy range as those used in the experiments.

TABLE I. Terms used to simulate the propagation of the ultrashort pulse.

	Description	Definition or value
λ	Peak laser wavelength	800 nm
ω_0	Carrier frequency	$2\pi/\lambda$
I	Intensity	$I = (1/2)n_0 c \epsilon_0 |A|^2$
z	Propagation axis	
τ	Retarded time	$\tau = t - z\,k_1$
k	Wave vector	$k(\omega) = n(\omega)\omega/c$
k_m	Dispersion coefficients	$k_m = \frac{\partial^m k(\omega)}{\partial \omega^m}\big|_{\omega_0}$
$\hat{D}_b$	Bound charge linear dispersion operator	$\hat{D}_b = \sum_{m=2}^{\infty} \frac{k_m}{m!}(i\,\partial_\tau)^m$
$\hat{T}$	Steepening operator	$\hat{T} = 1 + i\frac{1}{\omega_0}\partial_\tau$
$\hat{G}$	Drude dispersion operator	$\hat{G} = 1 + \frac{i}{\omega_0}g\partial_\tau$
g	Drude dispersion coefficient	$g = (-i\omega_0\tau_c)/(1 - i\omega_0\tau_c)$
σ	Absorption cross section	$e^2\tau_c/m_e n_0 \epsilon_0 c(1 + \omega_0^2\tau_c^2)$
$R(\tau)$	Raman response function	$R(\tau) = \frac{\tau_1^2 + \tau_2^2}{\tau_1\tau_2^2}e^{-\tau/\tau_2}\sin\tau/\tau_1$
τ_1	Raman response time	32 fs
τ_2	Raman response time	12.2 fs
f_r	Raman fraction of nonlinear polarization	0.18
n_0	Linear refractive index	1.45
k_2	GVD coefficient	361 fs^2 W^{-1}
n_2	Nonlinear refractive index	2.48×10^{-16} cm^2 W^{-1}
U	Band gap energy	9 eV
m_e	Electron rest mass	9.1×10^{-31} kg
τ_c	Electron collision time	Multiple values used

All experiments and computer simulations presented in this article were performed using fused silica as the sample material. The sample thickness of 200 μm in the computer simulations was chosen to match the sample thickness in the experiments. All other numerical parameters for the computer simulation (summarized in Table I) were taken from Ref. [19]. It was assumed that there is no initial spatiotemporal dependence in the pulse prior to propagation in the sample. This assumption is reasonable given that FROG traces without the sample, as well as those at low energies, do not show any signs of spatiotemporal dependences and yield unique solutions, which would not be the case otherwise.

IV. RESULTS AND DISCUSSION

This is the first work, to the authors' knowledge, in which both an experimentally measured beam profile and an experimentally determined pulse shape and phase are used in simultaneous simulations of ultrashort pulse propagation and ultrafast-laser induced plasma generation in a solid material. The results presented indicate that the inclusion of measured beam profiles and complex pulse structure in the initial conditions of the simulation greatly improved its accuracy and interpretive capability. Note that the following subsections, when stating damage thresholds, do so in terms of pulse energies for the pulses described in Sec. II. Whenever possible, damage thresholds are also given in terms of peak single-shot fluence on the front sample surface. Also, note that some of the subsections have different damage threshold measurements, as some were measured under different experimental conditions.

These damage thresholds are summarized as follows: 60 μJ (5.1 J/cm^2) for Secs. IV A and IV B, 45 μJ (3.8 J/cm^2) for Sec. IV C 2, and 55 μJ (4.7 J/cm^2) for Sec. IV C 3.

A. Damage threshold

The multishot damage threshold was determined in the experiment, by visual inspection, to be 60 μJ (5.1 J/cm^2). Since the sample was not translated in the experiment the surface was exposed to multiple ($\sim 10^7$) pulses of the same energy. This leads to cumulative effects when approaching the damage threshold. Every induced change in the optical properties of the sample leading to an increase in absorption will increase the modifying effect of the following pulse, lowering the damage threshold by approximately 25%. [35] The single-shot optical damage threshold is therefore expected to be around 80 μJ (6.8 J/cm^2). In the simulation, single-shot damage was assumed when the free-electron density anywhere in the sample exceeded the critical electron density of 10^{21} cm^{-3}.

The single-shot damage threshold calculated by the simulations depends sensitively on the free-carrier optical effects of plasma defocusing and absorption. In particular, the inclusion of the Drude correction operator $\hat{G}$ in the NLSE [Eq. (1)] is found to play a critical role in propagation dynamics and in determination of whether damage occurs in the bulk. These considerations are summarized in Fig. 2, which shows the simulated damage thresholds over a variety of possible collision times. Specifically, three calculated damage threshold plots are shown. The solid (black) curve shows the complete
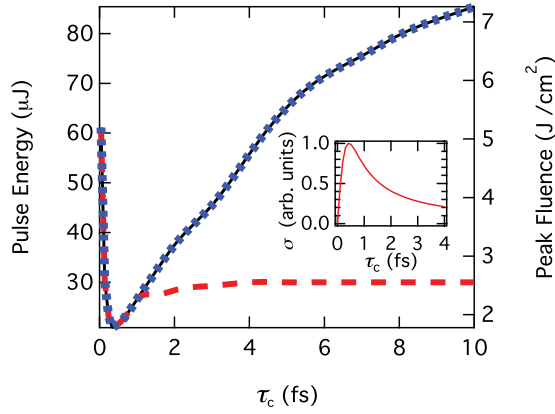
FIG. 2. (Color online) Single-shot damage thresholds (surface and bulk) as a function of collision time as determined by simulation for the full solution of Eq. (1) [solid (black) line], the solution of Eq. (1) where the operator $\hat{G} = 1$ [dashed (red) line], and the front surface damage threshold [dotted (blue) line]. Inset: Normalized Drude absorption cross section σ as a function of collision time for an 800-nm field in fused silica.

damage threshold (surface and bulk) for which the free-carrier dispersion operator $\hat{G}$ is fully included in Eq. (1), while the dashed (red) curve shows the complete damage threshold if $\hat{G}$ is taken to be unity (a common approximation for pulse widths >100 fs). The dotted (blue) line shows the damage threshold only for the front surface of the sample. Note that the general shape of the damage threshold curves, which all reach a minimum at approximately $\tau_c = 0.42$ fs, is dictated by the collision-time dependence of the absorption cross section σ, which peaks at approximately $\tau_c = 0.42$ fs. Note also that when the operator $\hat{G}$ is taken to be unity the damage threshold never exceeds 30 μJ (2.5 J/cm^2). Since simulated damage thresholds (surface or bulk) of energies less than 60 μJ (5.1 J/cm^2) directly contradict the experimental measurement, one must conclude that the full Drude dispersion term can significantly influence the accuracy of computer simulations, even for pulse widths of more than 100 fs. Generally, the importance of the Drude correction operator increases as the pulse width decreases. However, dynamic pulse processes, such as self-focusing and filamentation, can dramatically alter the initial pulse shape and even reduce the spatially local pulse widths by an order of magnitude. Therefore, even though the initial pulse widths in this work are all of the order of 140 fs, nonlinear effects will create a multitude of spatially local pulse widths during propagation, thereby providing an excellent test for the applicability of this corrective term. These are the first results of their kind to measure in experiment and validate by simulation the physics contained in the Drude correction operator.

In terms of the physics involved, the critical difference between the models used to calculate the solid (black) and dashed (red) lines in Fig. 2 is whether plasma absorption and defocusing were capable of halting self-focusing before free-carrier densities $>10^{21}$ cm^{-3} were generated in the bulk. When the full Drude correction operator $\hat{G}$ was included in Eq. (1), self-focusing in the bulk was halted at lower intensities and the generated plasma densities were of the order of 10^{20} cm^{-3}. Hence, damage for this case occurred only on the front surface,

and not in the bulk, and therefore matches the surface damage threshold exactly. When simulations assume that the Drude dispersion operator $\hat{G} \approx 1$ [dashed (red) line], self-focusing is allowed to continue and plasma densities $>10^{21}$ cm^{-3} are generated in the bulk for pulse energies of 30 μJ (2.5 J/cm^2) or higher, at the approximate self-focusing length of $z_{sf} = \pi w_{xy}^2/\lambda\sqrt{P/P_{cr} - 1}$, where P is the peak pulse power and $P_{cr} = \lambda^2/8\pi n_0 n_2$ is the critical power. Since the single-shot threshold is estimated from experiment to be 80 μJ (6.8 J/cm^2), Fig. 2 suggests an approximate collision time of the order of 10 fs for the results presented. Therefore a 10-fs collision time is assumed hereafter for all simulation results.

The corrective ability of the $\hat{G}$ operator to halt self-focusing and prevent damage is further demonstrated in Fig. 3. This figure shows the peak plasma density in the $y = 0$ and $x = 0$ planes for the cases of 30 μJ and 80 μJ pulses. Note that if $\hat{G} \approx 1$, Figs. 3(a) and 3(b), the damage threshold is
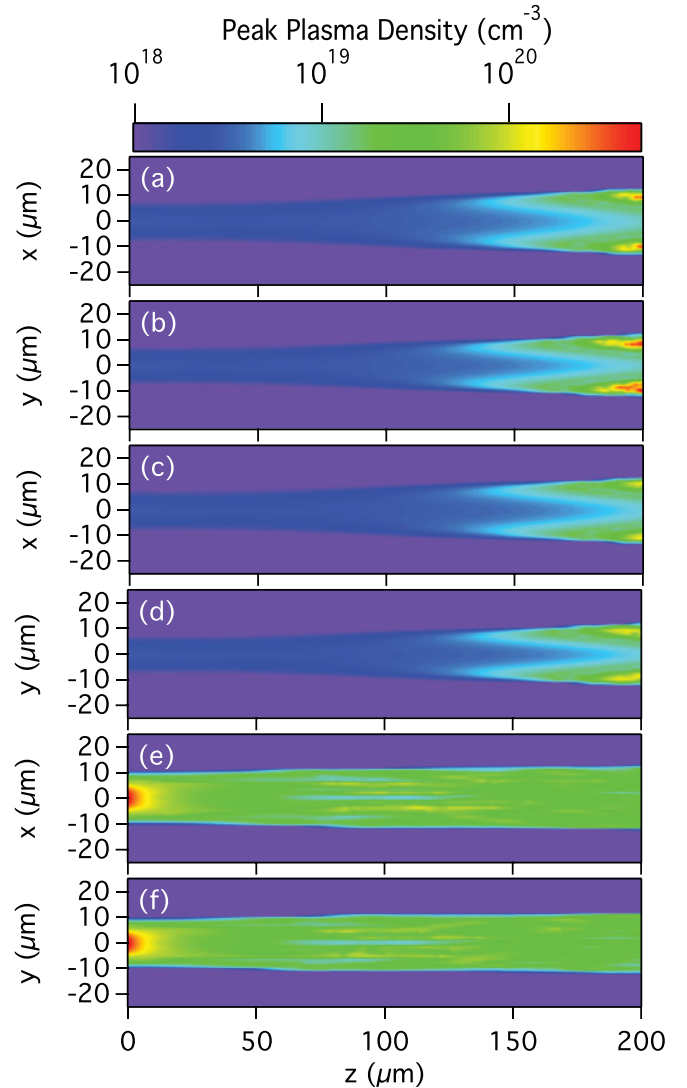

FIG. 3. (Color online) Peak plasma densities generated in the x-z ($y = 0$) and y-z ($x = 0$) planes for (a, b) the 30-μJ pulse without Drude dispersion corrections, (c, d) the 30-μJ pulse with Drude dispersion corrections, and (e, f) the 80-μJ pulse with Drude dispersion corrections.

reached near the end of the sample, whereas in Figs. 3(c) and 3(d), self focusing, laser-energy absorption, and the resulting ionization yield are limited by the effects of the $\hat{G}$ operator. This limiting effect is even more influential for higher pulse energies, since the pulse self-focuses at earlier points in the sample, as demonstrated by the case of the 80-μJ pulse [Figs. 3(e) and 3(f)]. Here the plasma density approaches the damage threshold on the front surface and then maintains values consistently in the range of 10^{19}–10^{20} cm^{-3}. Although plasma densities of the order of 10^{20} cm^{-3} are not typically associated with permanent structural damage, they have been associated with type I damage (nonstructural refractive index modifications that can be annealed by heating) [2]. The accumulation of these impurities can increase from one pulse to the next, leading to multipulse type II (structural) damage.

We note that, despite the sensitivity of the calculated surface damage threshold on the chosen collision time (see Fig. 2), the peak plasma densities achieved in the bulk did not vary significantly as a function of the collision time, maintaining values consistently in the range of 10^{19}–10^{20} cm^{-3} for all values of τ_c. The primary difference in the bulk between simulations using the determined $\tau_c = 10$ fs and simulations using $\tau_c < 3$ fs was that energy was more easily absorbed on the wings of the beam for lower collision times, broadening the plasma channels shown in Fig. 3 and decreasing the transmitted energy by 10% or more.

The 3D shapes and locations of material modifications are not possible to visualize from the 2D plots in Fig. 3 if cylindrical beam symmetry is not present. However, Fig. 4 shows a 3D isometric surface plot for the plasma density value of 10^{20} cm^{-3} (type I modifications) for the 80-μJ-pulse, single-shot simulation as a function of position in the sample. Note that, as in Figs. 3(e) and 3(f), Fig. 4 shows a type I modification on the front ($z = 0$) surface, but also multiple scattered modifications in the middle of the sample where the pulse self-focuses. Here the role of asymmetries in the spatiotemporal pulse structure are the most obvious, leading to numerous and specific modifications that are impossible to predict using cylindrical beam symmetry. Taken together, the scope of these modifications comprises a roughly circular
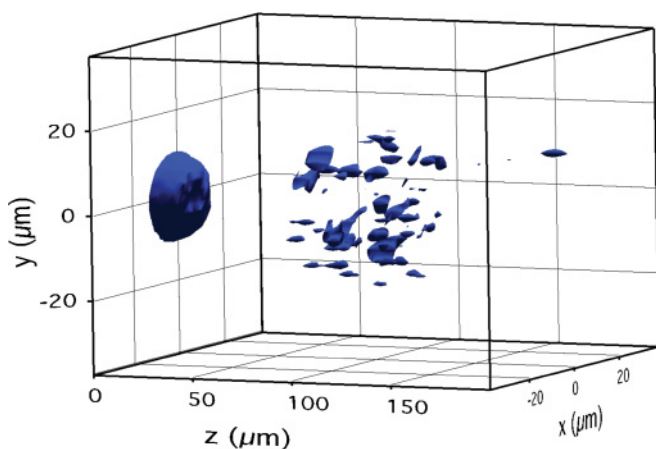
area of radius $\geqslant 20$ μm. If the later pulses in a multishot experiment gradually convert these type I modifications into type II structural damage, it is reasonable to expect that the energy transmission in a single-shot experiment will be higher than in an experiment involving exposure to 10^7 such pulses due to absorption and scattering by damage sites. This causes spatial dependence of the transmitted beam energy and will significantly alter any measurement of the far field for pulse energies above the multipulse damage threshold.

B. Beam profiles

To further examine the optical effects of the undercritical electron plasma, the measured beam profiles were compared with beam profiles from simulations using the corresponding input pulse energies. The experimentally measured and corresponding simulation beam profiles are shown in Fig. 5. The measured input beam profile is far from that of an ideal Gaussian beam. This offers a significant test of the agreement between experiment and simulation, once the far-field beam
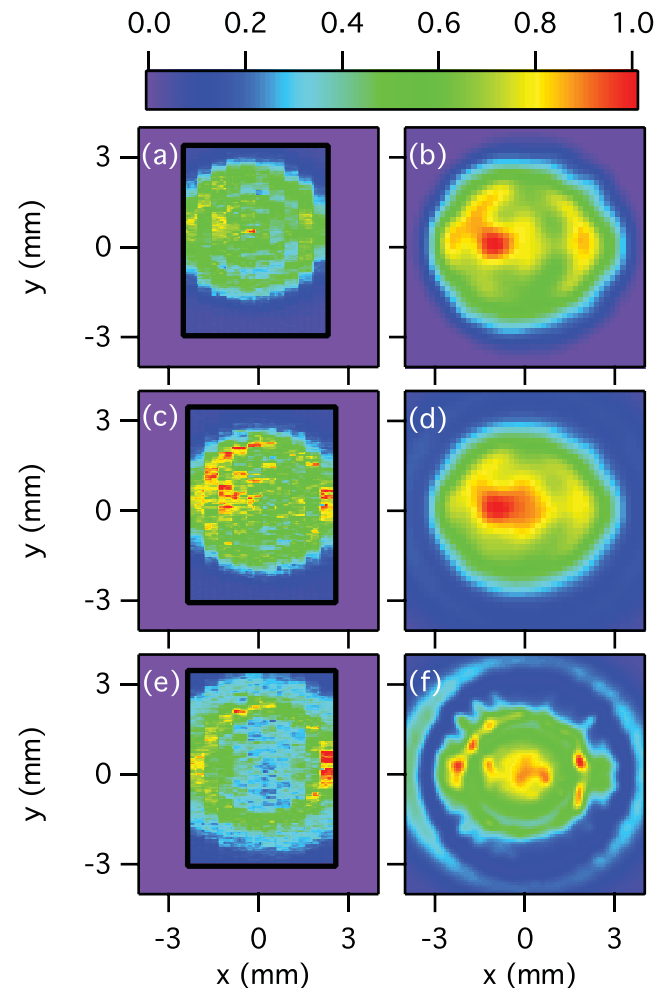

FIG. 5. (Color online) Normalized beam profiles. (a) measured beam profile before the first lens. (b) Simulated beam profile before the first lens. (c) Measured beam profile with a pulse energy of 10 μJ. (d) Simulated beam profile with a pulse energy of 10 μJ. (e) Measured beam profile for 80 μJ. (f) Ssimulated beam profile for 80 μJ.

FIG. 4. (Color online) Isometric surface plot of the peak plasma density value, 10^{20} cm^{-3}, as a function of the spatial coordinates in the material, for the case of an 80-μJ single-shot laser pulse.

profiles are compared. These simulations used a collision time of 10 fs and predicted a single-shot damage threshold of 80–85 μJ (6.8–7.2 J/cm^2). Also, the numerical field at the rear surface of the sample was inverse Fourier transformed to model the recollimating lens in the experiment. Here the field was integrated over time to produce a beam profile. A representative sample of measured beam profiles is shown together with their corresponding simulated beam profiles in Fig. 5. Measured and simulated beam profiles are shown before the lens [Figs. 5(a) and 5(b)] and after the sample for energies of 10 μJ [Figs. 5(c) and 5(d)] and 80 μJ [Figs. 5(e) and 5(f)].

The simulated beam profiles indicate that for pulse energies lower than 50 μJ, the high-fluence center region gains prominence over the features on the wings. The diffraction ring, as seen in the experimental beam profiles, fades in comparison with the center. For pulse energies higher than 50 μJ the opposite effect is observed, as a clear ring develops while the center region is reduced in relative fluence [Figs. 5(e) and 5(f)]. An interesting detail is the development of hot spots in this ring, which was seen in both the experimental and the simulated beam profiles for pulse energies of 30 μJ and higher. Note that the hot spots in the diffraction ring are only visible because the pulse propagation simulation allowed for asymmetric beam profiles in the input field. If cylindrically symmetric beam profiles had been assumed, then those details would be impossible to reproduce.

Although the single-shot simulations do predict a reduction in relative fluence at the beam center for energies exceeding the damage threshold [Fig. 5(f)], they still predict a hot spot at the beam center. This feature is not present in the corresponding experimental measurement [Fig. 5(e)], which shows a near-total reduction of the fluence at the beam center. The contradiction is likely due to the cumulative multipulse effects on material damage discussed in the previous subsection. If one uses the single-shot type I damage plots in Fig. 4 as an indicator of where multipulse damage sites will congregate, then most of the beam energy within a radius of up to 25 μm will not be transmitted through the sample. As a crude attempt to model this effect, one can multiply the numerical field at the end of the sample by a unit-step function $\theta(25\,\mu\text{m} - r)$, where r is the radial beam coordinate, effectively eclipsing the high-energy beam center. Figure 6(a) shows the simulated single-shot beam profile of the 80-μJ pulse immediately after the sample, with the dashed white circle indicating the transition of the applied unit-step function. Figure 6(b) shows

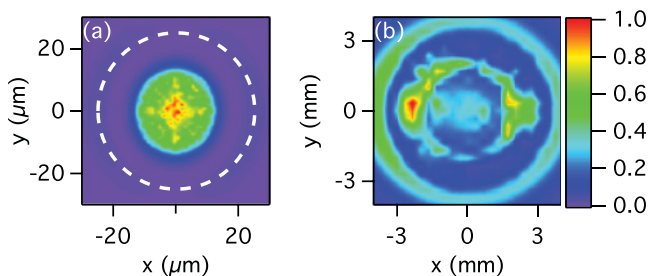the spatial Fourier transform of the numerical field represented in Fig. 6(a) to simulate propagation through the recollimating lens. Note that the relative fluence at the beam center is now 70% lower than that of the peaks and, therefore, improves the agreement with Fig. 5(e).

C. Comparison of retrieved fields from FROG traces to fields from computer simulation

To investigate the change in pulse shape due to interaction with the sample, SHG FROG was used, which measured high-dynamic-range traces by using a technique (multi-SHG-FROG) introduced in Ref. [36]. The fields are then retrieved from the multi-SHG-FROG traces and are compared to the fields obtained from the simulations. In the results of both experiment and simulation, FROG traces from pulses approaching the damage threshold are complicated by the presence of spatiotemporal dependences. However, it will also be shown that using an appropriate aperture allows for the retrieval of the temporal pulse amplitude, although not the temporal phase. This demonstrates that meaningful comparisons can still be made between experiment and simulation even with spatiotemporal dependence in the field, thus providing an additional test for the models of laser-plasma interaction.
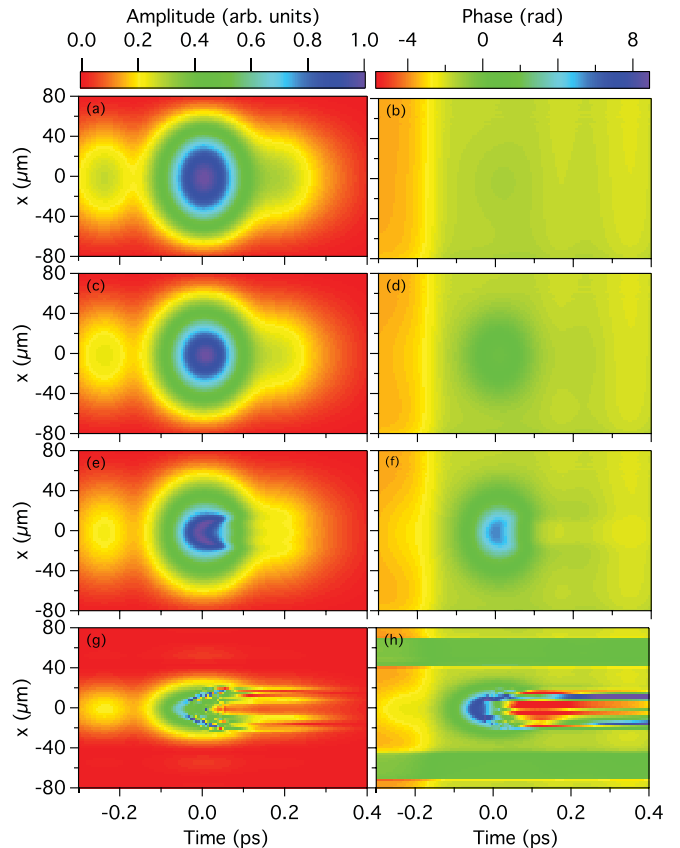

FIG. 6. (Color online) (a) Normalized simulated beam profile of the 80-μJ pulse immediately after the sample and (b) simulated 80-μJ beam profile after the recollimating lens if a 25-μm radial block [see white circle in (a)] is applied immediately after the sample.

FIG. 7. (Color online) Amplitude and phase of the complex field at $y = 0$ after the sample. Amplitude and phase (a, b) for 1 μJ input pulse energy, (c, d) for 10 μJ input pulse energy, (e, f) for 22 μJ input pulse energy, and (g, h) for 50 μJ input pulse energy.

1. Fields from simulation

The amplitude and phase after the sample for different input pulse energies in the $y = 0$ plane of the pulse are shown in the first and second columns in Fig. 7, respectively. With increasing input energy the pulse develops spatiotemporal inhomogeneities that can be seen in both the amplitude and the phase plots. The pulse shape does not vary as a function of x for energies under 22 μJ, but it will be shown later that

spatiotemporal dependences are often harder to identify in the amplitude than they are in the phase. As shown in Fig. 7, the phase does not vary as a function of x for 1 μJ, while for higher energies a region at the center of the pulse develops in which the phase depends strongly on the position in the beam. The amplitude and phase for the 10-μJ case show the onset of self-focusing and the development of a spatiotemporal dependence. For higher pulse energies, pulse filamentation can be observed as induced spatiotemporal dependences of the field in the form of hot spots. These dependences increase with increasing pulse energy as the filaments form earlier in the sample.

In order to investigate the effects of the restrictions applied to the field by the optics and smaller apertures, the field after the sample was Fourier transformed, an aperture was applied, and then the field after the sample was back Fourier transformed. These processes correspond to recollimating with a lens after the sample, aperturing using an iris, and focusing into the nonlinear crystal that is used in the SHG-FROG.

While the field shown in Fig. 8(a) is only representative of the whole beam at higher input pulse energies due to the strong spati-temporal dependences, the change to the field when passing through a 1-in. optic [Fig. 8(b)] can be clearly observed. Since the spatiotemporal dependences are greatly reduced when a small aperture is used, Fig. 8(c) can been seen as a representation of the on-axis field at the center of the beam. It is noteworthy that the observed phase change is greatly reduced by the aperture and that the amplitude shows, for higher energies, a dip at the former center of the pulse. This behavior must be distinguished from pulse splitting as a result of nonlinear effects. The effect seen here is due to the change induced to the field upon passing through optical elements later in the beam path. Pulse splitting was not observed inside the sample.
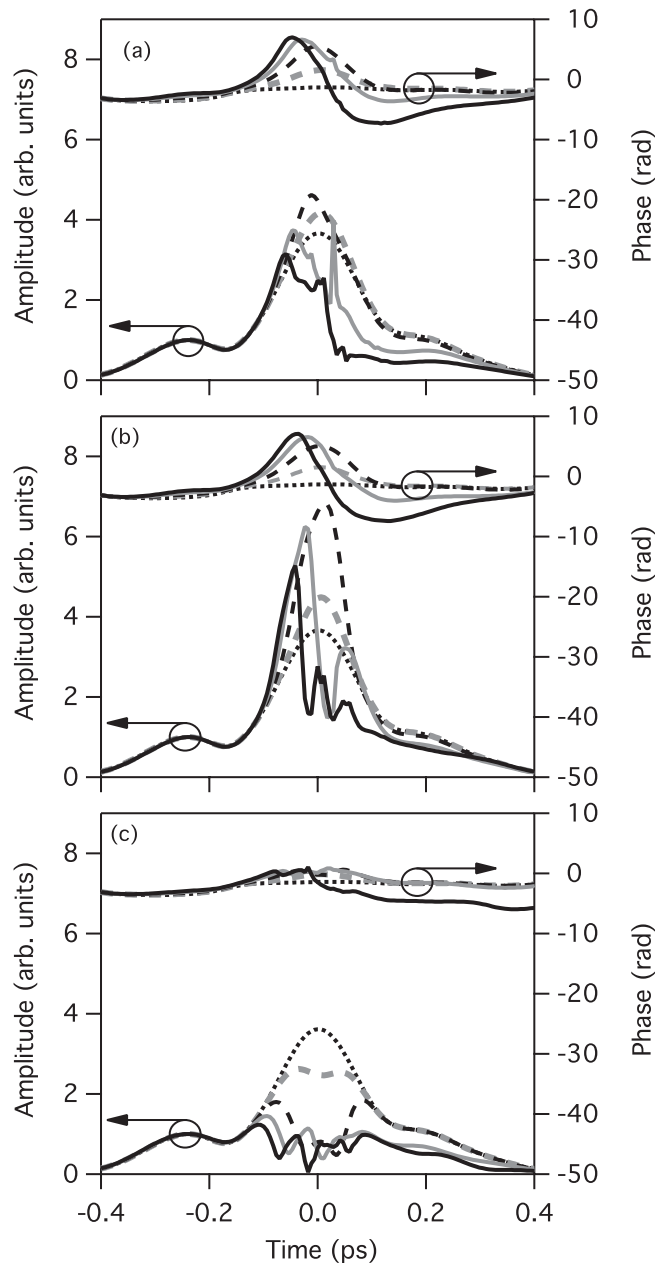

FIG. 8. Amplitude and phase of the field at the center of the beam (a) at the rear sample surface, (b) when a 25.4-mm (1-in.) aperture is applied, and (c) when a 4-mm aperture is applied. All amplitudes are normalized to the small front pulse at the left. Plots of different colors represent initial pulse energies of 1 μJ [dotted (black) curve], 10 μJ [dashed (gray) curve], 22 μJ [dashed (black) curve], 35 μJ [solid (gray) curve], and 50 μJ [solid (black) curve].
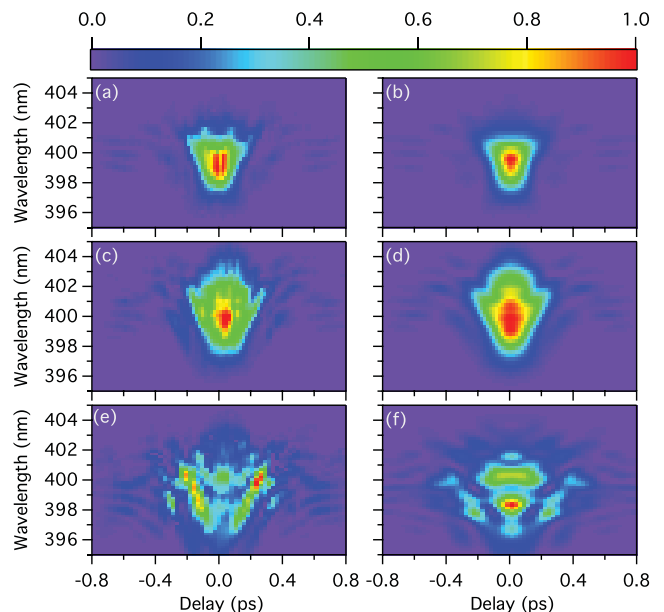

FIG. 9. (Color online) Measured and retrieved FROG traces for a pulse energy of (a, b) 10 μJ, (c, d) 40 μJ, and (e, f) 45 μJ. The destruction threshold of the sample was observed at 45 μJ (3.8 J/cm^2).

2. FROG traces from fields with spatiotemporal dependences

The presented computer simulations predict that pulses with energies approaching the damage threshold will have strong spatiotemporal dependences. Since the FROG retrieval process assumes a field with no x-y dependence, FROG traces from fields with spatiotemporal dependences do not yield a unique solution and often cannot be retrieved by this method. FROG traces shown in Fig. 9 show features that are not matched by the retrieval process and are best explained by the presence of strong spatiotemporal dependences. Figure 9 illustrates the change in FROG traces for pulse energies approaching the destruction threshold. The measured FROG traces in Fig. 9 show a dramatic change in form as the damage threshold is approached, as do the retrieved solutions, even though the experimental and retrieved traces clearly differ. The unretrievability of the traces is as predicted from computer simulations. The destruction threshold for this series was observed at 45 μJ (3.8 J/cm^2).

3. FROG traces from an apertured field

To reduce the spatiotemporal dependences in the field, the beam was apertured after the recollimating lens. FROG traces measured from the apertured field are shown in Fig. 10 and provide unique solutions that are shown in Fig. 11. Computer simulations demonstrate that the application of this aperture causes a significant loss of temporal phase information once the FROG trace is taken and that only the amplitude is retrieved in a meaningful way.

Figure 10 shows FROG traces from an apertured beam at different pulse energies with the matching autocorrelation signals and FROG traces found from the retrieved solution. The destruction threshold for this sequence was 55 μJ
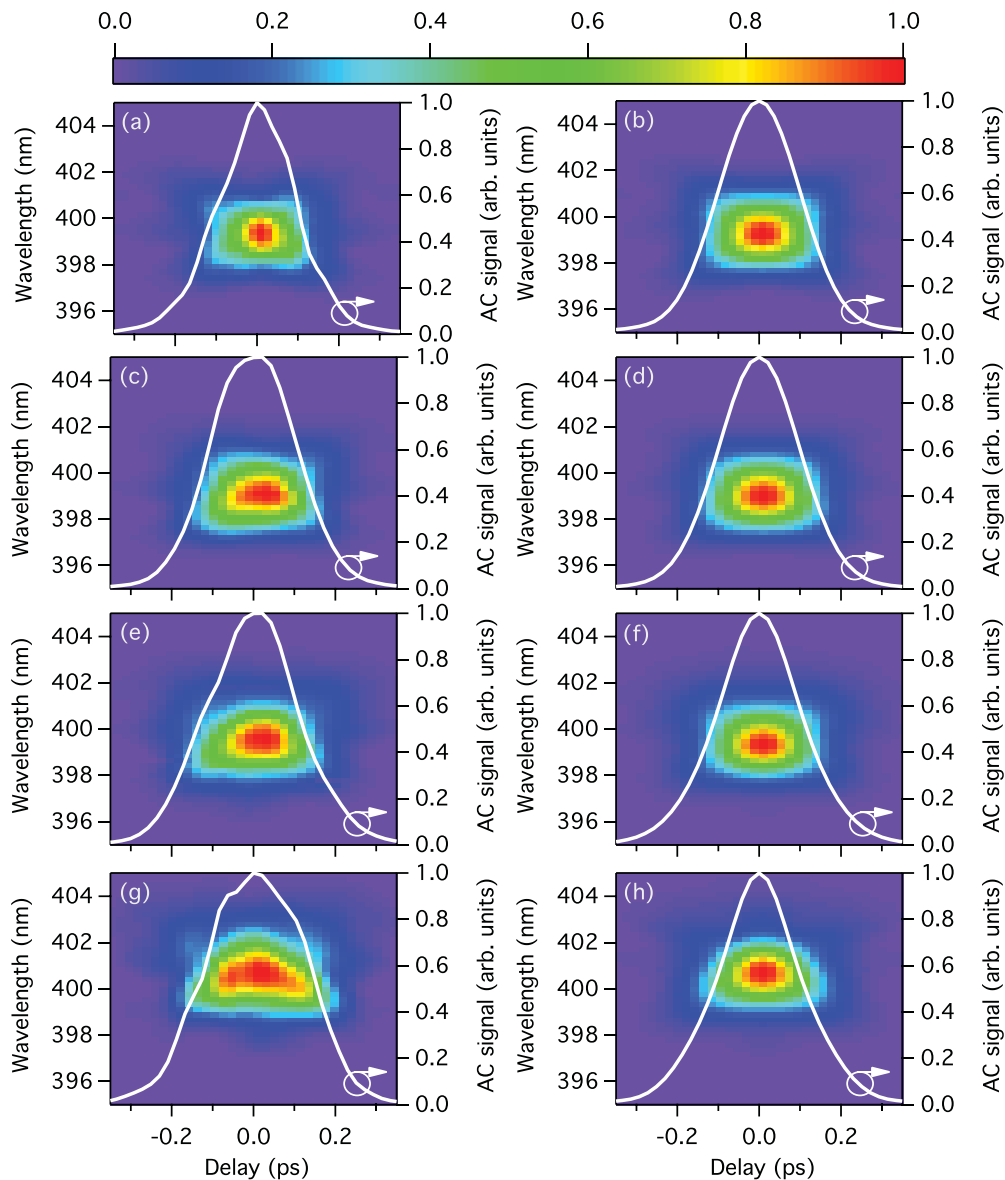

FIG. 10. (Color online) Measured FROG traces with the corresponding autocorrelation signals (solid line) and FROG traces found from the solution for an apertured beam. (Measured and retrieved FROG traces for a pulse energy of (a, b) 1 μJ, (c, d) 10 μJ, (e, f) 35 μJ, and (g, h) 46 μJ. The destruction threshold for this sequence was 55 μJ (4.7 J/cm^2). Complex field solutions for this set are shown in Fig. 11.
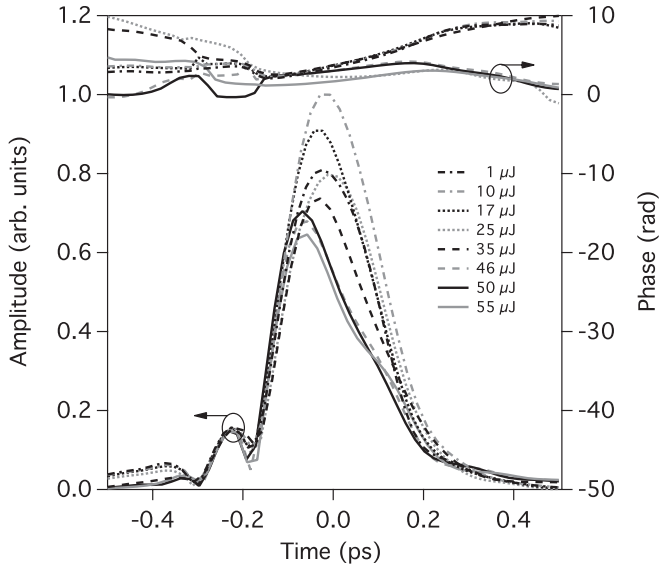
FIG. 11. Complex field amplitude (bottom plots) and phase (top plots) retrieved from FROG traces (shown in Fig. 10) measured for different pulse energies. The front of the pulse is on the left (earlier in time). Errors for the retrieval processes are listed in Table II.

(4.7 J/cm^2). Again, at energies close to the destruction threshold, significant differences between measured and retrieved FROG traces become apparent. These differences are considerably less than those observed when using the full beam but are, nonetheless, still present. This indicates that even though the spatiotemporal dependences have been reduced, they are not eliminated.

The retrieved fields for this experiment are shown in Fig. 11, while the errors associated with the retrieval process are listed in Table II. The retrieved fields at higher energies, as well as the contrast ratio of the pulse peak to the prepulse amplitude, are all decreased for apertured beams, while the phase does not show any sign of self phase modulation. Retrievals from artificial FROG traces show that the phase information is lost when strong spati-temporal dependences are present. Simulations also indicate that using an aperture to reduce spatiotemporal dependences greatly reduces the phase modulation in the center of the pulse.

TABLE II. G_{error} and offset compensation (OC) for the retrieval process of the complex fields in Fig 11.

Pulse energy (μJ)	Trace dimensions	G_{error}	OC
1	256×128	0.00319	0.0115
10	256×128	0.00417	0.0135
17	256×128	0.0036	0.0105
25	256×128	0.0041	0.008
35	256×128	0.00623	0.01
46	256×128	0.0051	0.011
50	256×128	0.00536	0.0095
55	256×128	0.0062	0.01

A likely explanation for the increase in the peak power for low energies is self-focusing. Computer simulations show that the beam is self-focusing at the pulse center ($\tau = 0$) for pulse energies in excess of 10 μJ. The decrease in the peak power for higher energies is explained by the increased role of plasma defocusing and absorption near the temporal center, as well as self-focusing of the prepulse. The resulting spatiotemporal dependences lead to an increase in beam width at the pulse center ($\tau = 0$) and an increased energy loss at the aperture.

The amplitudes of the fields were normalized to the small prepulse at the left, since nonlinear and plasma effects have a comparatively small effect on the behavior of the prepulse, but this feature is, in all cases, well above the background noise level. Experimental results shown in Figs. 10 and 11 were conducted using a laser system at the Laboratoire Hubert Curien of the Université Jean Monnet in Saint Ètienne.

V. CONCLUSION

To investigate ultrafast light-material interaction near the damage threshold, the high-dynamic-range multi-FROG technique was combined with measured beam profiles to analyze ultrashort high-energy laser pulses that had been propagated through a 200-μm-thick fused silica sample. Experiments were performed with pulse energies under the destruction threshold of the sample, an important regime in which postmortem investigations cannot be used. The comparison of beam profiles and pulse shapes, for both experiment and simulation, as a function of pulse energy provides significant insight into laser-plasma interactions and the evolution of the laser pulse. The combined data on ultrafast pulse propagation through undercritical laser-induced plasmas demonstrate the following.

(1) The use of a measured beam profile together with a measured temporal shape in computer simulations yields an improved agreement with experiment that would not be possible if symmetries in the simulated field had been assumed.

(2) It is demonstrated by experiment and simulation that the Drude dispersion operator $\hat{G}$, as derived in Ref. [30], is necessary to accurately model ultrafast pulse plasma dynamics due to rapidly changing plasma densities and steep pulse fronts that occur during the propagation process. This effect is critical to pulse evolution, as it is shown by simulation to prevent bulk damage and enable filamentation for the presented experiment.

(3) When approaching the damage threshold, nonlinear optical and plasma effects induce spatiotemporal dependences in the field, thus causing discrepancies between multishot and single-shot beam profiles, as well as causing the field to be unretrievable by an unapertured FROG trace.

(4) An apertured field will be retrievable from FROG traces, but only the amplitude is reproduced in a meaningful way. Measured and simulated amplitudes retrieved from apertured fields show a similar quantitative behavior when approaching the damage threshold, as measured by the ratio of the peak amplitude to the amplitude of the prepulse. Therefore, it is still possible to extract meaningful information about laser-plasma interactions from the far field.

The disagreements between experimental and simulated far-field beam profiles and retrieved fields suggest that a single-shot (translated sample) version of the experiment may

be required for quantitative prediction. Translating the sample would additionally determine where in the material single-shot damage occurs. Also, a more detailed knowledge of the initial and final experimental fields may be required. Experimental measurements designed to measure the complete complex field as a function of space and time (see, e.g., the recent methods in Refs. [37–41]) will reduce the need to assumeg an initial field with no spatiotemporal dependences or to use apertured FROG traces. Additionally, recent investigations into the possible role of high-order nonlinear optical effects [42–44], ionization by multichromatic pulses [45], and the influence of phenomenological parameters (such as the free-carrier collision time and the effective electron mass) [46] may also allow for further improvements in predamage calculations.

[1] C. L. Arnold, A. Heisterkamp, W. Ertmer, and H. Lubatschowski, Opt. Express **15**, 10303 (2007).

[2] A. Couairon, L. Sudrie, M. Franco, B. Prade, and A. Mysyrowicz, Phys. Rev. B **71**, 125435 (2005).

[3] R. R. Gattass, L. R. Cerami, and E. Mazur, Opt. Express **14**, 5279 (2006).

[4] D. Giguère, G. Olivié, F. Vidal, S. Toetsch, G. Girard, T. Ozaki, J.-C. Kieffer, O. Nada, and I. Brunette, J. Opt. Soc. Am. A **24**, 1562 (2007).

[5] L. Jiang and H.-L. Tsai, Appl. Phys. Lett. **87**, 151104 (2005).

[6] L. Jiang and H.-L. Tsai, J. Heat Transfer **128**, 926 (2006).

[7] B. Rethfeld, V. V. Temnov, K. Sokolowski-Tinten, P. Tsu, D. von der Linde, S. I. Anisimov, S. I. Ashitkov, and M. B. Agranat, J. Opt. Technol. **71**, 348 (2004).

[8] A. Rosenfeld, M. Lorenz, R. Stoian, and D. Ashkenasi, Appl. Phys. A **69**, S373 (1999).

[9] C. B. Schaffer, A. Brodeur, J. F. Garcia, and E. Mazur, Opt. Lett. **26**, 93 (2001).

[10] C. B. Schaffer, A. O. Jamison, and E. Mazur, Appl. Phys. Lett. **84**, 1441 (2004).

[11] C. B. Schaffer and E. Mazur, Opt. Photonics News **12**, 20 (2001).

[12] X. Zhu, A. Yu. Naumov, D. M. Villeneuve, and P. B. Corkum, Appl. Phys. A **69**, S367 (1999).

[13] I. M. Burakov, N. M. Bulgakova, R. Stoian, A. Rosenfeld, and I. V. Hertel, Appl. Phys. A **81**, 1639 (2005).

[14] L. R. Cerami, E. Mazur, S. Nolte, and C. B. Schaffer, in *Ultrafast Optics*, edited by R. Trebino and J. Squier (Trafford, Bloomington, IN, 2007), pp. 1–1.

[15] A. Horn, E. W. Kreutz, and R. Poprawe, Appl. Phys. A **79**, 923 (2004).

[16] V. Kudriagov, E. Gaizauskas, and V. Sirutkaitis, J. Opt. Soc. Am. B **22**, 2619 (2005).

[17] A. Saliminia, N. T. Nguyen, S. L. Chin, and R. Vallee, Opt. Commun. **241**, 529 (2004).

[18] J. R. Gulley, S. W. Winkler, and W. M. Dennis, Opt. Eng. **47**, 054302 (2008).

[19] S. W. Winkler, I. M. Burakov, R. Stoian, N. M. Bulgakova, A. Husakou, A. Mermillod-Blondin, A. Rosenfeld, D. Ashkenasi, and I. V. Hertel, Appl. Phys. A **84**, 413 (2006).

[20] B. C. Stuart, M. D. Feit, S. Herman, A. M. Rubenchik, B. W. Shore, and M. D. Perry, Phys. Rev. B **53**, 1749 (1996).

[21] C. B. Schaffer, A. Brodeur, and E. Mazur, Meas. Sci. Technol. **12**, 1784 (2001).

[22] L. Sudrie, A. Couairon, M. Franco, B. Lamouroux, B. Prade, S. Tzortzakis, and A. Mysyrowicz, Phys. Rev. Lett. **89**, 186601 (2002).

[23] L. Sudrie, M. Franco, B. Prade, and A. Mysyrowicz, Opt. Commun. **191**, 333 (2001).

[24] O. Efimov, S. Juodkazis, and H. Misawa, Phys. Rev. A **69**, 042903 (2004).

[25] J. R. Vázquez de Aldana, C. Méndez, L. Roso, and P. Moreno, J. Phys. D **38**, 2764 (2005).

[26] B. C. Stuart, M. D. Feit, A. M. Rubenchik, B. W. Shore, and M. D. Perry, Phys. Rev. Lett. **74**, 2248 (1995).

[27] D. von der Linde and H. Schuler, J. Opt. Soc. Am. B **13**, 216 (1996).

[28] I. H. Chowdhury, X. Xu, and A. M. Weiner, Appl. Phys. Lett. **86**, 151110 (2005).

[29] R. Trebino, *Frequency-Resolved Optical Gating: The Measurement of Ultrashort Pulses* (Springer, New York, 2002).

[30] J. R. Gulley and W. M. Dennis, Phys. Rev. A **81**, 033818 (2010).

[31] B. Rethfeld, Phys. Rev. Lett. **92**, 187401 (2004).

[32] L. V. Keldysh, Sov. Phys. JETP **20**, 1307 (1965).

[33] B. H. Christensen and P. Balling, Phys. Rev. B **79**, 155424 (2009).

[34] A. Q. Wu, I. H. Chowdhury, and X. Xu, Phys. Rev. B **72**, 085128 (2005).

[35] C. B. Schaffer, N. Nishimura, and E. Mazur, Proc. SPIE **3451**, 2 (1998).

[36] S. W. Winkler, Ph.D. thesis, University of Georgia, Athens (2009).

[37] P. Bowlan, P. Gabolde, A. Shreenath, K. McGresham, R. Trebino, and S. Akturk, Opt. Express **14**, 11892 (2006).

[38] P. Bowlan, P. Gabolde, and R. Trebino, Opt. Express **15**, 10219 (2007).

[39] P. Bowlan, P. Gabolde, M. A. Coughlan, R. Trebino, and R. J. Levis, J. Opt. Soc. Am. B **25**, A81 (2008).

[40] J. Cohen, P. Bowlan, V. Chauhan, and R. Trebino, Opt. Express **18**, 6583 (2010).

[41] L. Xu, E. Zeek, and R. Trebino, J. Opt. Soc. Am. B **25**, A70 (2008).

[42] P. Béjot, J. Kasparian, S. Henin, V. Loriot, T. Vieillard, E. Hertz, O. Faucher, B. Lavorel, and J.-P. Wolf, Phys. Rev. Lett. **104**, 103903 (2010).

[43] M. Kolesik, E. M. Wright, and J. V. Moloney, Opt. Lett. **35**, 2550 (2010).

[44] M. Kolesik, D. Mirell, J.-C. Diels, and J. V. Moloney, Opt. Lett. **35**, 3685 (2010).

[45] J. R. Gulley, in *Laser-Induced Damage in Optical Materials: 2010*, edited by G. J. Exarhos, V. E. Gruzdev, J. A. Menapace, D. Ristau, and M. J. Soileau (SPIE, Bellingham, WA, 2010), Vol. 7842, p. 78420U [http://link.aip.org/link/?PSI/7842/78420U/1].

[46] V. Gruzdev, in *Laser-Induced Damage in Optical Materials: 2010*, edited by G. J. Exarhos, V. E. Gruzdev, J. A. Menapace, D. Ristau, and M. J. Soileau (SPIE, Bellingham, WA, 2010), Vol. 7842, p. 784216 [http://link.aip.org/link/?PSI/7842/784216/1].